Supporting Information for "Quantitative visualization of two-phase flow in a fractured porous medium"

Zhen Liao[1,2], Russell L. Detwiler[3], Esther Cookson[3], Wanjun Lei[1,2], Yi-Feng Chen[1,2]

[1]State Key Laboratory of Water Resources Engineering and Management, Wuhan University, Wuhan 430072, China

[2]Key Laboratory of Rock Mechanics in Hydraulic Structural Engineering of the Ministry of Education, Wuhan University, Wuhan 430072, China

[3]Department of Civil and Environmental Engineering, University of California Irvine, Irvine, CA, United States

Contents of this file

1. Text S1 to S3
2. Figures S1 to S7

Additional Supporting Information (Files uploaded separately)

1. Movies S1 to S4 show the phase evolution of primary and secondary drainage-imbibition processes in Experiments FFH and MFH, respectively.

Text S1. Procedure of processing the porous glasses.

The square porous glass plates were ordered from Rudong Shundao Glass Instrument Factory, China, and all porous glass plates were processed as follows (Figure S1): (1) Due to the large difference between thickness ($\sim$ 6$\pm$1 mm) and length scale (149$\pm$1 mm), a small amount of warping occurred during fabrication inducing a long-wavelength variation. To remove the long-wavelength variation of the porous plates, the top and bottom surfaces were sanded (Norton ProSand 80 secured to a flat glass surface). This process gradually removed sintered glass beads until the surfaces were relatively flat; they retained the small-scale roughness induced by the porosity of the surfaces. After sweeping the powder off the surfaces by a soft brush, the porous glasses were flushed with DI water for several minutes and soaked for 2 hours in DI water with ultrasonication and then dried in a vacuum oven at 45 ℃ overnight. (2) In order to seal the edges and create a cavity, the porous glasses were placed in a specially designed mold, and dyed epoxy was then poured into the mold along the 4 edges. We used West System 105 Epoxy Resin / 206 Slow Hardener. The epoxy penetrated several millimeters into the porous glass to enhance sealing but did not influence the central region of the porous plates (see Figure S2). Note, the epoxy also created a rim surrounding the porous surface that created a cavity between the porous surface and the supporting window when the test cell was assembled. We used Fisher Scientific Sudan Black BP109-10, which is an oily dye that is insoluble in water, to dye the epoxy to facilitate visualization of the epoxy-filled region. After 24 hours of curing at room temperature, the epoxied porous plates were removed from the mold. (3) The epoxy rim surrounding the bottom of each surface were sanded flat and to uniform thickness using P80 sandpaper and then polished using P400 sandpaper.

The resulting smooth bottom surface ensured water-tight contact with the bottom PVC gasket to prevent leakage. The 4 edges of the epoxied porous glasses were then sanded to match the size of the smooth glass surface, which ensured the porous surface mated well with the smooth glass to simplify sealing of the no-flow boundaries and flow manifolds. The epoxied and sanded porous plates were then cleaned and dried again through the same cleaning and drying process. Finally, the epoxied regions around the edges of the porous surfaces were smoother than the un-epoxied regions because the pores were filled with epoxy. This resulted in very small fracture apertures around the perimeter of the fracture when the test cell was assembled. To provide a pathway for air to enter the central region of the fracture, we created 3 wedge-shaped grooves equally distributed along the sides of the fractures connected to the flow manifolds (Figure S2). This allowed us to focus on the flow in the central fracture, where the matrix porosity is unaffected by epoxy and boundary constraints.

Text S2. Aperture estimation based on Laplace-Young relationship.

For a two-phase flow in fracture, we know that the capillary head (Ψ) is a function of the principal radii of curvature and the interfacial tension according to the Laplace-Young equation (Glass et al., 1998):

$$\Psi = \frac{\gamma}{\rho_{\mathrm{w}} g}\left(\frac{1}{r_1} + \frac{1}{r_2}\right) \tag{S1}$$

where γ is the interfacial tension, r_1 is the radius of aperture-induced curvature and r_2 is the radius of in-plane curvature. By assuming that the fracture walls are symmetric about a mean plane and neglecting the influence of local convergence/divergence angle (β) of the fracture walls, r_1 can be calculated as (Yang et al., 2012):

$$r_1 = \frac{b}{2\cos\theta} \tag{S2}$$

where b is the fracture local aperture, and θ is the contact angle of the fluid-fluid-fracture system. Actually, another assumption underlying equation (S2) is that the contact angle θ is the same on the top and bottom fracture surfaces. While in our experimental model, we noticed that the contact angle on the smooth glass and the porous glass (FF or MF) are not exactly the same (Figure S5 (a)), thus equation (S2) should be modified as follows (see Figure S5 (b)):

$$r_1 = \frac{b}{\cos\theta_1 + \cos\theta_2} \tag{S3}$$

in which θ_1 and θ_2 are the contact angle of water and air on the smooth glass and the porous glass, respectively, and their measured value are shown in Figure S5 (a).

What's more, the influence of r_2 is often assumed to be negligible (i.e., r_2 is much larger than r_1) (Glass et al., 1998), therefore the capillary head Ψ can be approximated as:

$$\Psi = \frac{\gamma(\cos\theta_1 + \cos\theta_2)}{\rho_w g b} \tag{S4}$$

Or the local fracture aperture b can be estimated by the applied capillary head Ψ:

$$b = \frac{\gamma(\cos\theta_1 + \cos\theta_2)}{\rho_w g \Psi} \tag{S5}$$

Text S3. Results of Experiment FFV

In order to investigate how gravity affects the cyclic drainage and imbibition processes, the vertical experiment (Experiment FFV) was conducted in the same FF fractures. Phase distributions at the end of each pressure step are shown in Figure S6, in which the capillary head Ψ was defined relative to the fracture's centerline. Because the bottom manifold and connected tubing were closed off, the air can only invade into the fracture through the top edge during the primary drainage process. Rather than a relatively uniform capillary head Ψ applied to the horizontal fracture in Experiment FFH, the Ψ applied to the vertical fracture actually distributed linearly along the fracture length (from Ψ to Ψ-152 mm). This linear distribution suppressed the air to vertically invade into the lower part of the fracture when $\Psi \leq 426$ mm, as the actual capillary head applied to the lower part of the fracture is not big enough to overcome the capillary pressure. However, the water has a potential tendency to flow downward under its own gravity, thus facilitating the air to spread to the no-flow boundaries, resulting a wider invasion front than Experiment FFH. An intuitive understanding of this difference can be gained by comparing the air cluster pattern at step Ψ=401 mm in primary drainage (DR1) of Experiment FFV with step Ψ=398 mm in DR1 of Experiment FFH. As the Ψ continues to increase, the air finally breaks through the bottom edge of the fracture and invades the bottom manifold, causing some water that existed in the bottom manifold to be imbibed into the fracture and flow into the reservoir through the matrix. After that, with further increases in Ψ, air expanded towards the no-flow boundaries. During the imbibition processes, due to the effect of the gravity of water and the buoyancy of air, the air became relatively easy to displaced out from the top edge, thus less air was trapped in the lower part of the

fracture, and the overall residual air saturation at the end of the imbibition processes was lower than that in Experiment FFH.

Figure S7a shows Ψ plotted against $S_{\mathrm{w}}^{\mathrm{A}}$ for each cycle of Experiment FFV, which also exhibits significant hysteresis. Figure S7b shows the relationship between the estimated water and air relative permeabilities, $k_{\mathrm{r,w}}$ and $k_{\mathrm{r,a}}$, respectively, and the areal saturation $S_{\mathrm{w}}^{\mathrm{A}}$ of the water phase. By comparing the air relative permeability $k_{\mathrm{r,a}}$ of FFV with FFH, one can intuitively find that air is less permeable due to the effect of gravity, i.e., air is permeable ($k_{\mathrm{r,a}} > 0$) when $S_{\mathrm{w}}^{\mathrm{A}}$ is less than ~ 0.5 in Experiment FFV, while in FFH, air is permeable when $S_{\mathrm{w}}^{\mathrm{A}}$ is less than ~ 0.7.

Movie S1. Phase evolution of primary drainage and imbibition process in Experiment FFH.

Movie S2. Phase evolution of secondary drainage and imbibition process in Experiment FFH.

Movie S3. Phase evolution of primary drainage and imbibition process in Experiment MFH.

Movie S4. Phase evolution of secondary drainage and imbibition process in Experiment MFH.

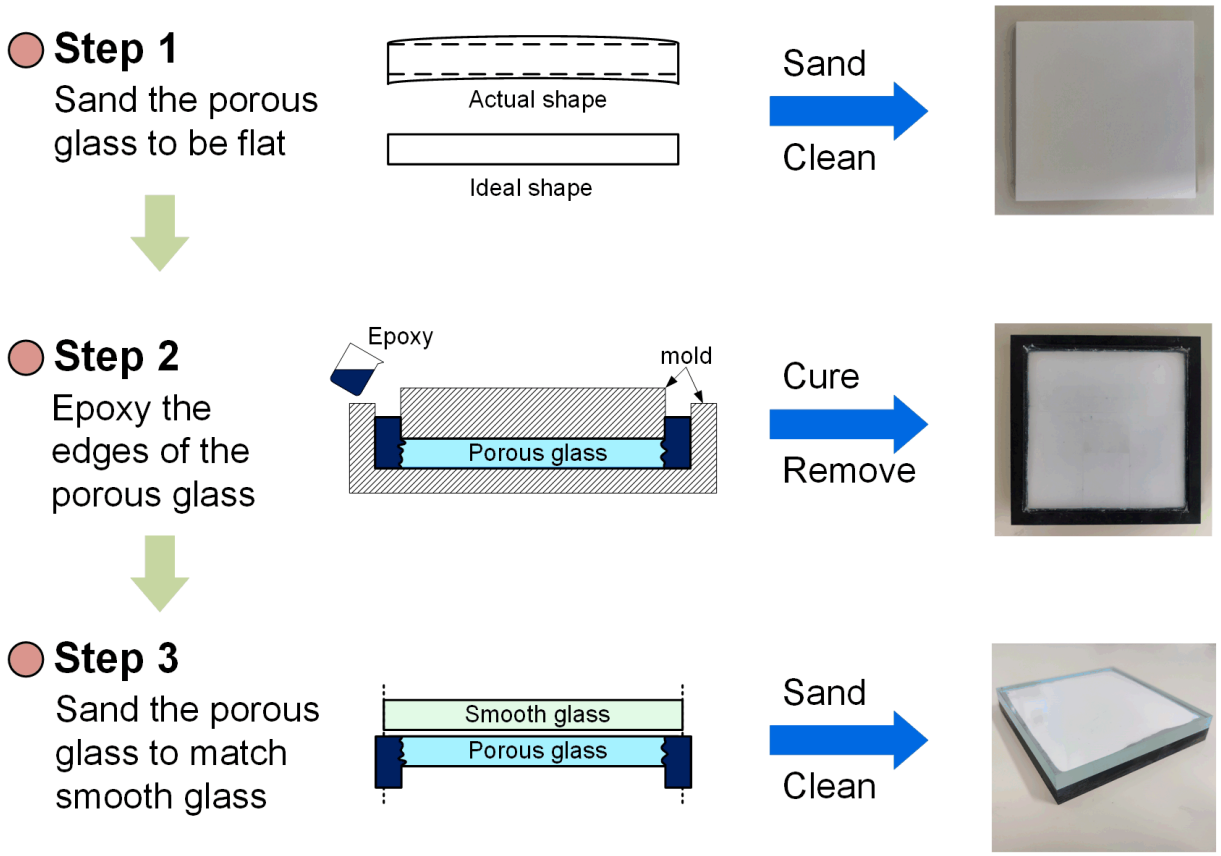

Figure S1. The procedure of processing the porous glasses.

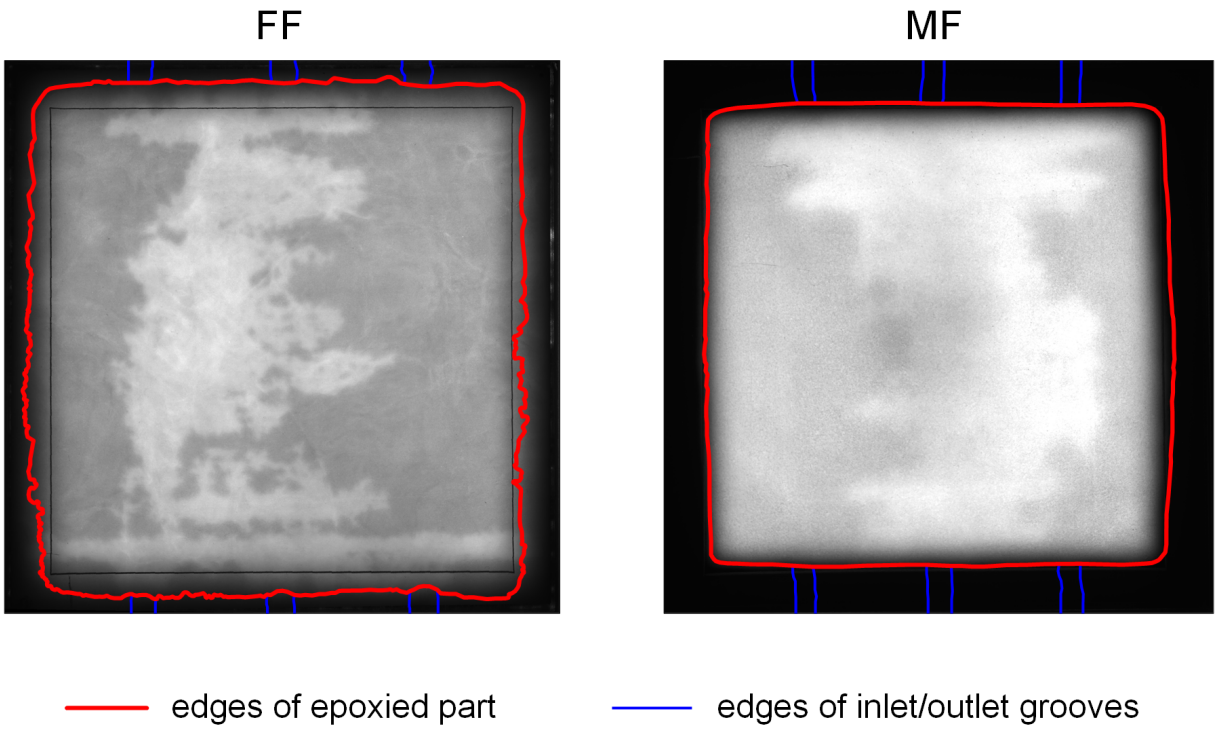

Figure S2. Edges of the epoxied part and inlet/outlet grooves of the FF and MF model. The ratios of projected area of the epoxied part to the projected area of the porous glass's top surface are about 18.59% and 30.15% for FF and MF model, respectively. The background raw images are corresponding to the end of the pressure steps at $\Psi = 398$ and 248 mm for FF and MF model, respectively.

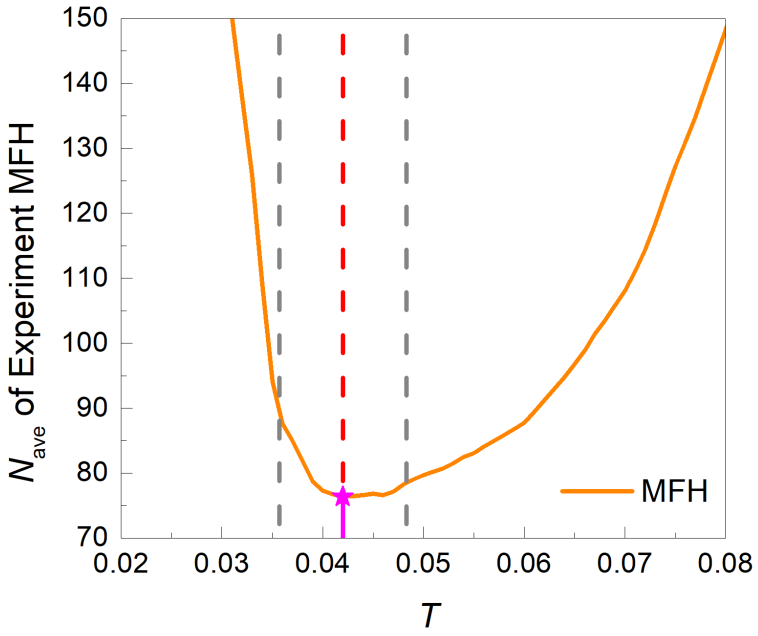

Figure S3. The N_{ave}-T plot of Experiment MFH. Plotting the average number of segmented air clusters, N_{ave}, versus the threshold values for Experiment MFH, T_{MFH}, also reveals distinct minima. The optimal threshold was $T^{\star}_{\text{MFH}} = 0.042 \pm 0.006$.

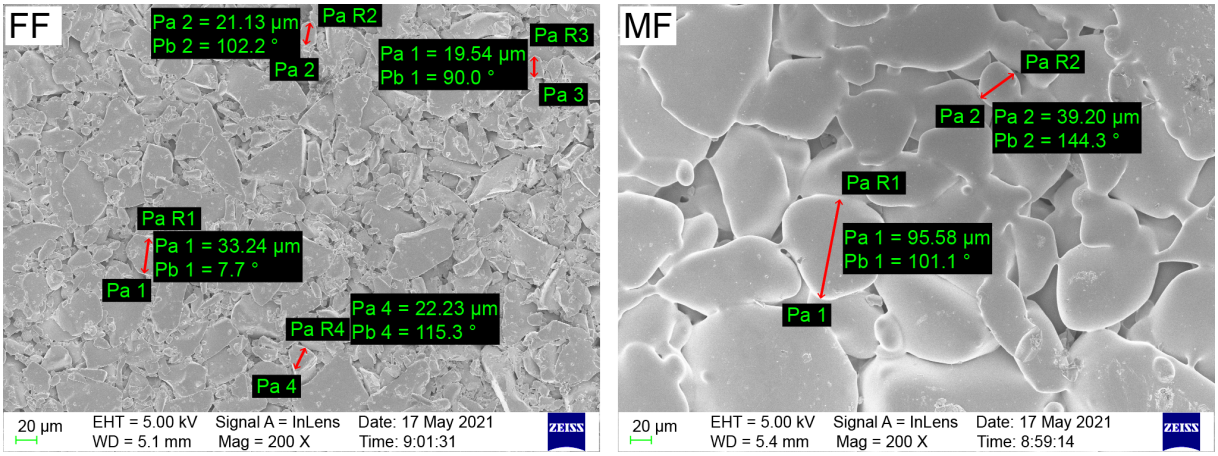

Figure S4. SEM images of the porous glasses. High resolution images of the surfaces of FF (fracture with fine pore-size matrix) and MF (fracture with medium pore-size matrix), captured by the field emission scanning electron microscopy (SEM) in Wuhan University, showing big difference of the sintered bead sizes between FF and MF.

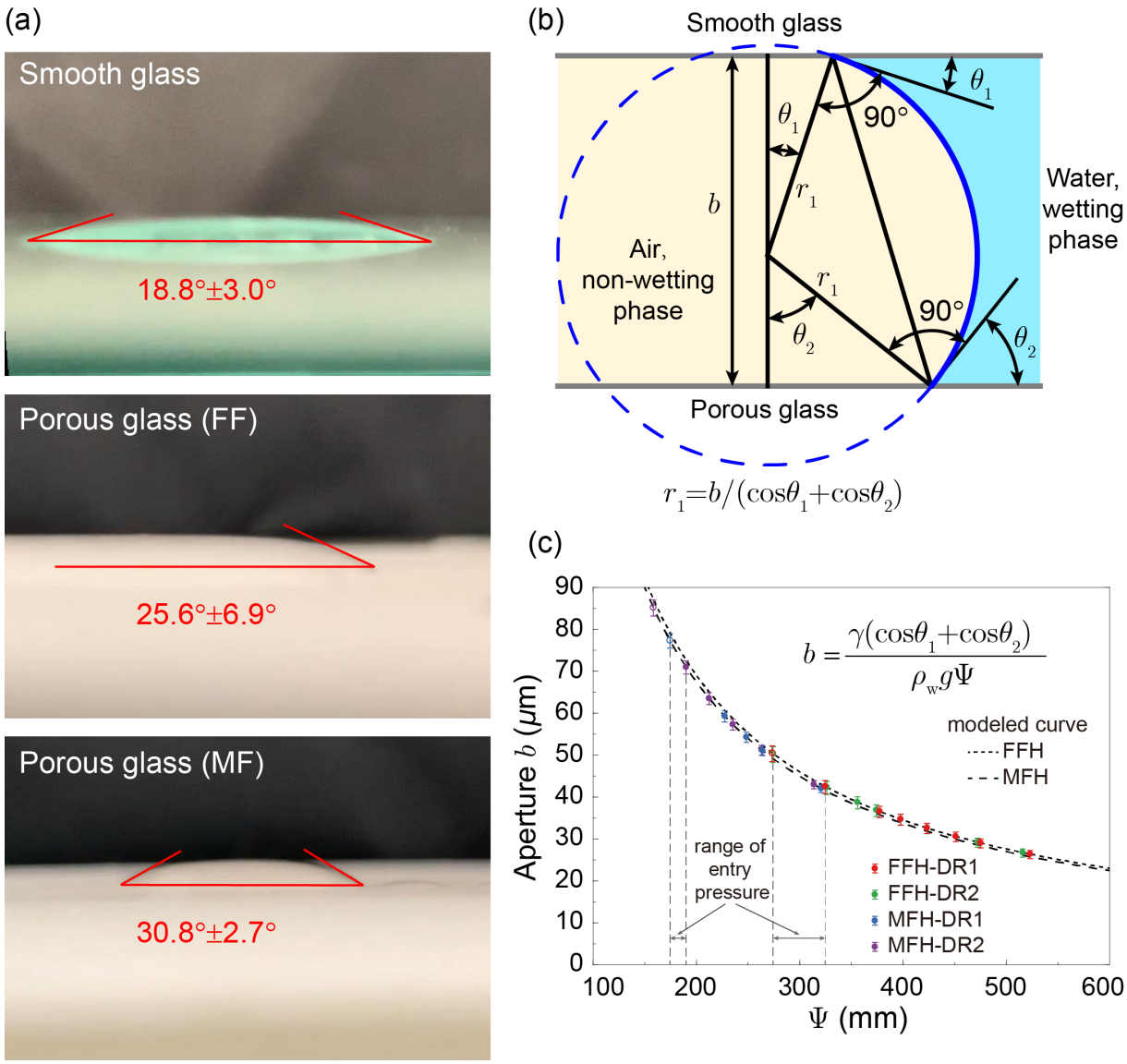

Figure S5. Aperture estimation based on Laplace-Young relationship. (a) Measured contact angles on the smooth glass and porous glass. (b) Cross-section illustration of a water-air interface within the fracture, showing the radius of aperture-induced curvature r_1 related to the fracture local aperture b and different contact angles on the smooth glass and porous glass (θ_1 and θ_2). (c) Estimated fracture local aperture b corresponding to the applied capillary head Ψ based on equation (S4) (modeled curves), in which the hollow and solid circles represent the experimental steps that air didn't invade or invaded into the fracture.

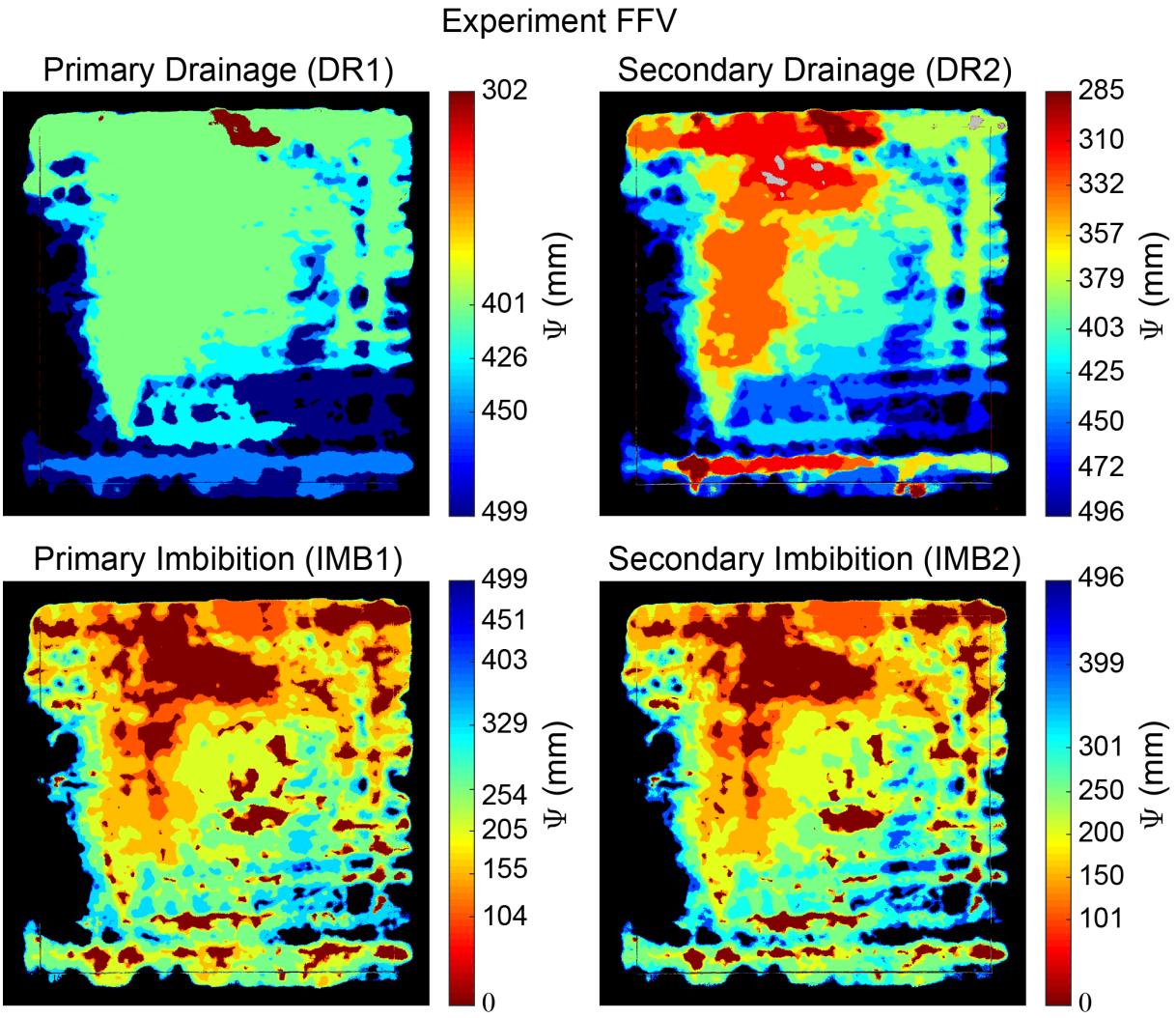

Figure S6. Phase evolution during cyclic drainage and imbibition processes of Experiment FFV. The colors reflect air occupancy at sequential values of Ψ during each step of the experiment, with warm colors indicating smaller values of Ψ and cool colors indicating larger Ψ; black regions remained water-filled at the breakthrough Ψ (final step of each experiment). The grey regions in the secondary drainage figures are regions that remained air-filled at the end of primary imbibition.

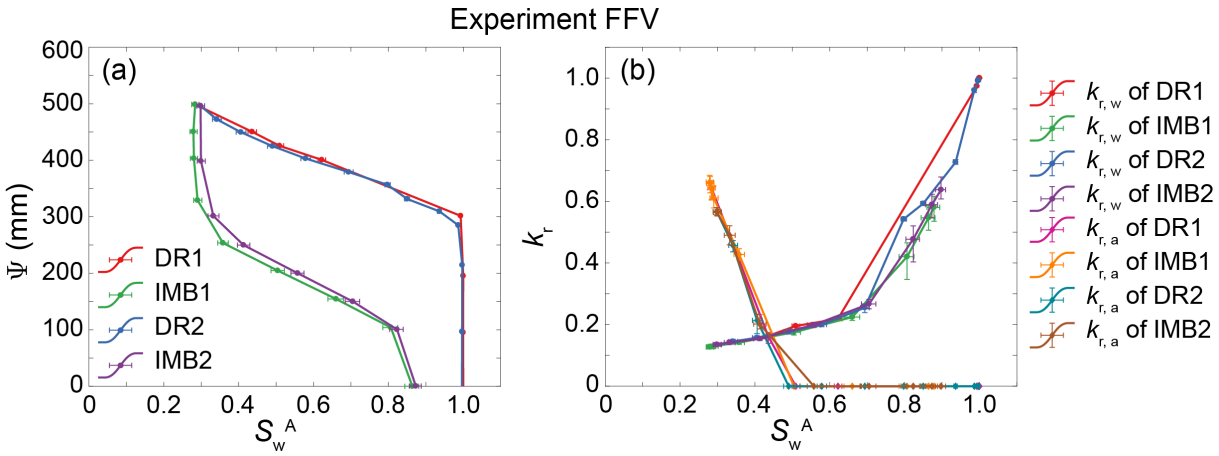

Figure S7. Relationship between applied capillary head Ψ and areal water saturation $S_{\mathrm{w}}^{\mathrm{A}}$ for Experiment FFV (a), and relationship between modeled relative permeability of water or air ($k_{\mathrm{r,w}}$, $k_{\mathrm{r,a}}$) and areal water saturation $S_{\mathrm{w}}^{\mathrm{A}}$ for Experiment FFV (b), in which $S_{\mathrm{w}}^{\mathrm{A}}$, $k_{\mathrm{r,w}}$ and $k_{\mathrm{r,a}}$ are the average values during the last 1 min in each step.

References

Glass, R. J., Nicholl, M. J., & Yarrington, L. (1998). A modified invasion percolation model for low-capillary number immiscible displacements in horizontal rough-walled fractures: Influence of local in-plane curvature. *Water Resources Research*, *34*(12), 3215-3234. doi: https://doi.org/10.1029/98WR02224

Yang, Z., Niemi, A., Fagerlund, F., & Illangasekare, T. (2012). A generalized approach for estimation of in-plane curvature in invasion percolation models for drainage in fractures. *Water Resources Research*, *48*(9), W09507. doi: https://doi.org/10.1029/2012WR011829